Letter Vol. 50, No. 5 / 1 March 2025 / Optics Letters 1457

Optics Letters

Non-iterative far-field synthetic aperture imaging via space-domain Kramers–Kronig relations

SHENG LI,[1,2,3] BOWEN WANG,[1,2,3] HAITAO GUAN,[1,2,3] QIAN SHEN,[1,2,3] QIAN CHEN,[1,3] AND CHAO ZUO[1,2,3,*]

[1]Smart Computational Imaging Laboratory (SCILab), School of Electronic and Optical Engineering, Nanjing University of Science and Technology, Nanjing, Jiangsu Province 210094, China
[2]Smart Computational Imaging Research Institute (SCIRI) of Nanjing University of Science and Technology, Nanjing, Jiangsu Province 210019, China
[3]Jiangsu Key Laboratory of Spectral Imaging & Intelligent Sense, Nanjing, Jiangsu Province 210094, China
*zuochao@njust.edu.cn

Received 10 December 2024; revised 17 January 2025; accepted 22 January 2025; posted 23 January 2025; published 18 February 2025

Non-interferometric synthetic aperture imaging (SAI) shows significant potential in Earth observation, astronomy, and remote sensing. However, these methods often involve time-consuming processes for wave field acquisition and iterative image reconstruction. In this Letter, we present a non-iterative far-field synthetic aperture imaging method, macroscopic space-domain Kramers–Kronig relations synthetic aperture imaging (MSKR-SAI). Unlike traditional macroscopic Fourier ptychography (FP), MSKR-SAI bypasses redundant iterations and requirements for highly overlapping images, reducing reconstruction time from 4.97 s to 0.17 s—a 26-fold speedup. By utilizing only six sub-aperture intensity images, MSKR-SAI reconstructs complex amplitude information and synthesizes the aperture in a fully determinist manner. Simulations and experimental results show a twofold resolution improvement with accurate detail recovery and minimal artifacts. Furthermore, MSKR-SAI maintains robustness even when the Kramers–Kronig relations are not strictly met. The combination of non-iterative reconstruction, noise resilience, and computational efficiency positions MSKR-SAI as a promising method for high-resolution, artifact-free far-field imaging.

https://doi.org/10.1364/OL.551414

Achieving high-resolution imaging is essential in optical remote sensing, where resolution enhancement is typically limited by the aperture size of the optical system. While increasing the aperture size can improve resolution, it also introduces significant manufacturing and processing challenges. Synthetic aperture techniques, commonly used in microwave radar, simulate a large virtual aperture by moving the antenna and applying coherent signal processing for high-resolution detection and imaging. However, optical detectors have slower response times than radar antennas, making it difficult to directly acquire phase information and complicating the implementation of conventional optical synthetic aperture methods.

Fourier ptychographic microscopy (FPM) is closely related to both non-interferometric phase retrieval and interferometric synthetic aperture imaging [1–4]. Unlike conventional methods that spatially scan the object with a narrow illumination beam, FPM uses a light-emitting diode (LED) array to provide variable-angle illuminations without the need for moving parts. The low-resolution images captured at different angles are synthesized in the Fourier space, surpassing the diffraction limit of the objective lens and effectively increasing the microscope's space–bandwidth product (SBP) [5,6].

Over the past decade, Fourier ptychography (FP) has gained widespread adoption for complex wave field reconstruction and synthetic aperture imaging in far-field detection [7,8]. Dong *et al.* demonstrated macroscopic Fourier ptychography at a distance of 0.7 m using LED illumination, with the reconstructed complex field enabling synthetic aperture imaging and digital refocusing [9]. Holloway replaced the LED with a highly coherent laser, enabling high-resolution imaging of diffuse targets and further advancing macroscopic Fourier ptychography techniques [10,11]. However, a major limitation of existing macroscopic FP methods is the time-consuming aperture scanning process for image acquisition and iterative reconstruction, both of which reduce imaging efficiency.

To achieve high spatiotemporal resolution in non-interferometric synthetic aperture imaging for far-field detection, previous efforts have mainly focused on reducing image acquisition time. Wu *et al.* introduced total variation (TV) regularization into the iterative process of macroscopic Fourier ptychography, reducing the required overlap from 39.1% to 25% [12]. Although TV regularization reduced the number of sub-aperture images and acquisition time, the complex iterative process increased reconstruction time. Illumination multiplexing combined with a camera array enables single-exposure, high-resolution imaging [13]. However, demultiplexing sub-aperture images adds complexity to the iterative process in illumination multiplexing, which increases reconstruction times and computational demands.

Recently, the Kramers–Kronig relations have attracted attention in non-interferometric quantitative phase imaging (QPI) due to their ability to decouple the real and imaginary

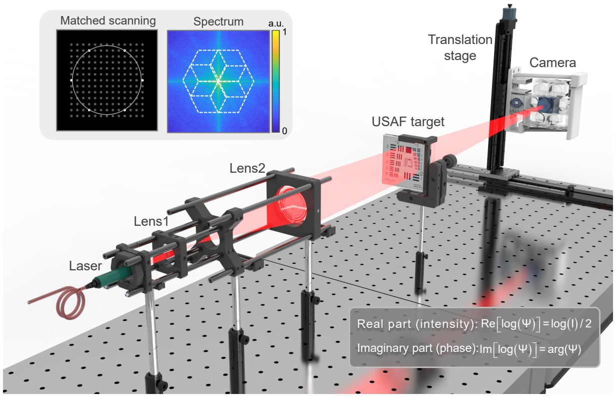

Fig. 1. Overview of the proposed method framework. Lens1 and Lens2 are utilized for modulating the laser to illuminate the target. Sub-aperture images are captured by the camera scanning with translation stage.

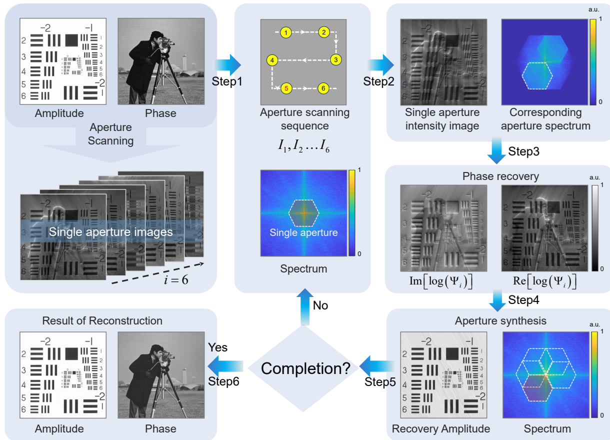

Fig. 2. Workflow of the reconstruction process of the MSKR-SAI method.

components of a complex function analytic in the upper half-plane (UHP) [14,15]. A method based on space-domain Kramers–Kronig relations converts spatial intensity variations into phase variations, enabling phase imaging from a single intensity measurement under oblique illumination [16–18]. While the Kramers–Kronig relations show promising potential for complex wave field reconstruction in far-field imaging [19], current methods with illumination control still face challenges in retrieving phase information from distant targets.

Here, we present a method for far-field complex wave field reconstruction and resolution enhancement via space-domain Kramers–Kronig relations. We propose a novel far-field synthetic aperture technique, macroscopic space-domain Kramers–Kronig relations synthetic aperture imaging (MSKR-SAI). This method leverages the aperture scanning characteristics of macroscopic imaging systems and applies the space-domain Kramers–Kronig relations for non-iterative phase recovery. Simulations with the U.S. Air Force (USAF) resolution target demonstrate a twofold improvement in resolution, and the reconstruction speed increases by 26-fold, from 4.97 s to 0.17 s. Furthermore, we evaluate the robustness of the method under varying measurement errors, highlighting its resilience in synthetic aperture imaging, even with deviations in sub-aperture positions.

The optical setup for our proposed method is shown in Fig. 1. For long-range imaging, the lens positioned after the target is used to satisfy the Fraunhofer diffraction condition. The sub-aperture is positioned in the Fourier domain to capture light information from different locations on the target. To meet the analytical conditions of the Kramers–Kronig relations, the transverse wave vector of the incident plane wave must align with the cutoff spatial angular frequency of the pupil function. We use a translation stage to scan the camera, aligning the edge of the sub-aperture with the spectral center and recording six sub-aperture intensity images. The imaging process can be described as follows:

$$I_m = \left| F^{-1}\left\{ (\Psi_m) \cdot P \right\} \right|^2, \tag{1}$$

where I_m is the intensity information at the mth position, Ψ_m is the corresponding complex amplitude, and P is the pupil function of a single aperture. The flow chart of phase recovery and synthetic aperture imaging utilizing the acquired sub-aperture images is depicted in Fig. 2. During the imaging process, amplitude information is captured by the imaging system in the form of intensity (as shown in Fig. 2, S1 in Supplement 1), while the corresponding phase information is lost.

To visually demonstrate the process of phase recovery and synthetic aperture imaging from an intensity image, we use the USAF 1951 resolution target as the intensity image and the Cameraman image as the phase image. The camera captures sub-aperture images of the target at six specific locations, as illustrated in Step 2. Notably, in the actual imaging system, the aperture shape is a polygonal configuration determined by the blades of the lens diaphragm (see Supplement 1, Note 1). Therefore, we calibrated the Fujinon HF75HA-1B lens, which was used in our imaging experiments, confirming that the aperture shape is a regular hexagon composed of six blades (as illustrated in Steps 3 and 4). For the square-integrable function $f(x)$ analytic in the UHP [14], its imaginary part can be expressed by the following formula:

$$\mathrm{Im}\left[f(x)\right] = -\frac{1}{\pi} p.v. \int_{-\infty}^{\infty} \frac{\mathrm{Re}\left[f(x')\right]}{x' - x} dx', \tag{2}$$

where $p.v.$ denotes the Cauchy principal value. The relationship of $f(x)$ is utilized to reconstruct the complex amplitude information from the intensity measurements. The amplitude Ψ of the sub-aperture can be expressed as follows:

$$\mathrm{Re}\left[\log(\Psi)\right] = \log(I)/2, \tag{3}$$

$$\mathrm{Im}\left[\log(\Psi)\right] = \arg(\Psi), \tag{4}$$

where $I = |\Psi|^2$. The real part is a logarithmic function of intensity, and the imaginary part is the phase of $\log(\Psi)$. Thus, the phase image can be recovered from the intensity image if the Kramers–Kronig relations hold between the real and imaginary parts of $f(x)$. The intensity image of Ψ can be interpreted as the intensity of a different electric field ε:

$$I(\boldsymbol{\gamma}) = |\Psi(\boldsymbol{\gamma})|^2 = |\varepsilon(\boldsymbol{\gamma})|^2, \tag{5}$$

$\boldsymbol{\gamma} = x\hat{\boldsymbol{x}} + y\hat{\boldsymbol{y}}$, and $\varepsilon(\boldsymbol{\gamma}) = \Psi(\boldsymbol{\gamma})e^{i\boldsymbol{k}_{inc}\cdot\boldsymbol{\gamma}}$, with $\boldsymbol{k}_{inc}$ representing the transverse wave vector. The complex function is written as follows:

$$\chi(\boldsymbol{\gamma}) = \log\left[\varepsilon(\boldsymbol{\gamma})\right] = \log\left[\Psi(\boldsymbol{\gamma})\right] - i\mathbf{k}_{inc}\cdot\boldsymbol{\gamma}, \tag{6}$$

whose real part is $\log(I)/2$ and the imaginary part is $\arg(\Psi) - i\boldsymbol{k}_{inc}\cdot\boldsymbol{\gamma}$. The real and imaginary components of the function $\chi(\boldsymbol{\gamma})$ obey the Kramers–Kronig relations when $\boldsymbol{k}_{inc}$ is the cutoff spatial angular frequency of a pupil function. This enables phase retrieval through intensity image analysis. In microscopy, this condition is called the "matched illumination condition" [20]. Correct recovery of low spatial frequency phase information is only achievable when the LED is precisely positioned at the edge of the objective's numerical aperture (NA) in frequency space [21,22]. Compared to other bright-field or dark-field images, these specific bright-field raw images contain the most information, especially valuable low-frequency phase data. Using matched annular illumination improves both recovery accuracy and reduces the number of raw images required [23]. In far-field imaging systems, this is achieved by precisely aligning the pupil margin of the imaging system with the spectrum center during aperture scanning, referred to as "matched scanning conditions." After computing the complex amplitudes for the six sub-aperture positions, we stitch and synthesize these amplitudes in the Fourier domain, as shown in Step 5 and Step 6, to obtain the synthetic aperture imaging result. Unlike the complex iterations required by Fourier ptychography, MSKR-SAI avoids the need for sub-aperture images with high redundancy as constraints. Instead, by directly obtaining the complex amplitude at each position from intensity images, the complex amplitudes of the six apertures are stitched together in the Fourier domain based on the weight coefficients of each aperture, enabling high-quality synthetic aperture imaging.

The MSKR-SAI method enables phase reconstruction based on a non-iterative approach, allowing its application in various fields. In far-field detection, performing morphology measurements of microscopic surface structures in a non-contact manner can further mitigate the impact of system vibrations on imaging (see Supplement 1, Note 2). Another key feature of the proposed method is its ability to non-iteratively reconstruct the complex amplitude in far-field imaging, simultaneously and efficiently achieving twice the optical resolution of a single aperture. To demonstrate the resolution enhancement, we set the numerical aperture (NA) of the sub-aperture to 0.08 and used red light with a wavelength of 653 nm as the coherent illumination source to simulate the U.S. Air Force resolution target for evaluating the system's resolution performance. We also simulated the effect of the difference between the actual aperture shape after calibration and the ideal circular aperture on the reconstruction results.

The hexagonal sub-aperture shape in the spectrum is shown in Fig. 3(a1), while Figs. 3(a2)–3(a3) display intensity images corresponding to the spectrum components intercepted by the hexagonal sub-aperture and the enlarged regions of interest. Due to the numerical aperture limitation, the resolvable line pair in the imaging result for the hexagonal sub-aperture corresponds to group 0, element 3. Figure 3(b1) illustrates the spectrum distribution resulting from the synthesis of six circular sub-apertures, while Figs. 3(b2)–3(b3) present the corresponding imaging results and the enlarged regions of interest. Under ideal sub-aperture shapes, the proposed method enhances the resolvable line pairs to group 1, element 3, doubling the resolution to twice that of a single aperture. Figure 3(c1) depicts the spectrum distribution of the synthesized hexagonal sub-aperture,

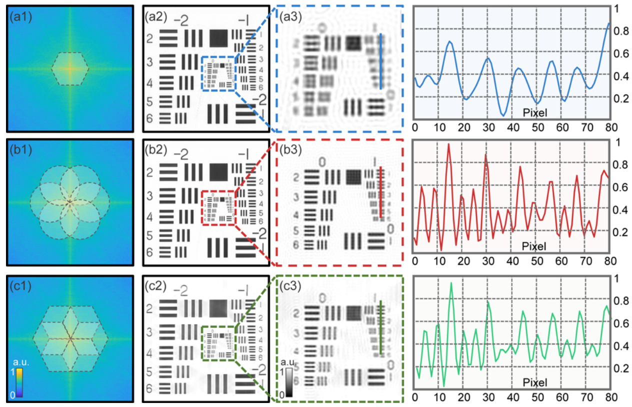

Fig. 3. Reconstruction results of the USAF resolution target with different aperture shapes. (a1) Spectrum distribution of a hexagonal sub-aperture. (a2)–(a3) Intensity images correspond to (a1) and enlarged regions of interest. (b1) Spectrum distribution resulting from the synthesis of six circular sub-apertures. (b2)–(b3) Intensity images correspond to (b1) and enlarged regions of interest. (c1) Spectrum distribution of the synthesized hexagonal sub-aperture. (c2)–(c3) Intensity images correspond to (c1) and enlarged regions of interest.

while Figs. 3(c2)–3(c3) show the corresponding reconstruction results and enlarged regions of interest. To the right of the enlarged region of interest is the corresponding line profile. The reconstruction result with six hexagonal apertures maintains the resolution enhancement, closely aligning with results achieved using six circular apertures. Furthermore, we compared our proposed method with far-field Fourier ptychography (see Supplement 1, Note 3). Unlike the iterative process in far-field Fourier ptychography, our method reduces computation time by nearly 26 times (from 4.97 s to 0.19 s), demonstrating its imaging efficiency due to its non-iterative nature.

In both microscopic and macroscopic imaging, the aperture edge must be strictly tangent to the center to satisfy the Kramers–Kronig relations. Deviations between the aperture edge and the center, to varying degrees, can lead to phase recovery errors, affecting the reconstruction of the complex wave field. We have developed a real imaging system to quantitatively analyze the impact of deviations between the aperture margin and the center on the reconstruction result. The imaging system, shown in Fig. 4(a), uses a 653 nm fiber laser (5 mW power) to illuminate the sample through a focusing lens. The system is positioned 1.5 m from the sample, and the imaging lens (Fujinon HF75HA-1B, 75 mm focal length, and an F-number adjustable from 2.8 to 16) is set to an F-number of 5.6. A translation stage (HGTA01150, 200 mm range of motion) drives an 8-bit CMOS camera (DMK33UX226, Imaging Source, with a resolution of 4000×3000 pixels and a pixel size of 1.85 μm) to scan and capture six sub-aperture images.

Figure 4(b1) presents the sub-images with the spectrum center located outside the aperture, while the corresponding reconstruction result, which exhibits noticeable errors, is displayed in Fig. 4(b3). In Fig. 4(c1), the sub-images where the aperture is precisely tangent to the center are shown, with the corresponding reconstruction result provided in Fig. 4(c3). The artifact-free, high-resolution reconstruction verifies that the exact tangency of the sub-aperture to the center satisfies the Kramers–Kronig relations. Lastly, Fig. 4(d1) illustrates the sub-images with the

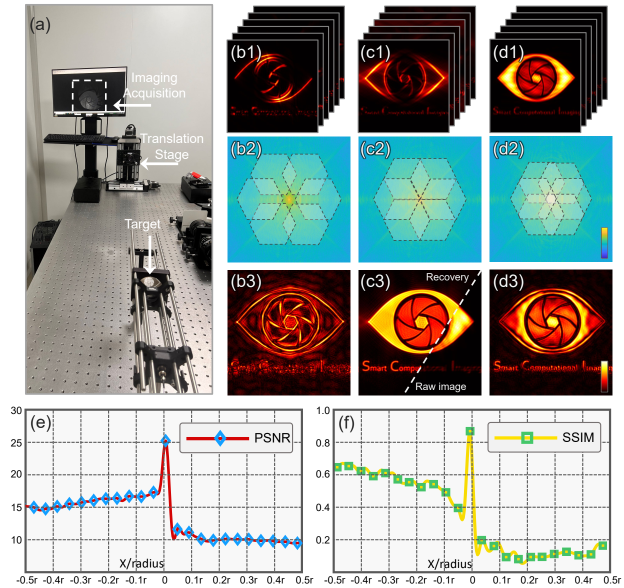

Fig. 4. Comparative experiments on a designed target sample. (b1) Sub-images with the spectrum center located outside the aperture. (b2)–(b3) Spectrum and corresponding reconstruction result of (b1). (c1) Sub-images where the aperture is precisely tangent to the center. (c2)–(c3) Spectrum and corresponding reconstruction result of (c1). (d1) Sub-images with the spectrum center located within the aperture. (d2)–(d3) Spectrum and corresponding reconstruction result of (d1). (e)–(f) PSNR and SSIM of the reconstruction results at various deviation distances.

spectrum center located within the aperture, and the corresponding reconstruction result is depicted in Fig. 4(d3). Compared to the reconstruction results when the spectrum center is outside the aperture, those with the center within the aperture boundary enhance resolution, though with certain artifacts that impact image quality. An objective quantitative assessment based on the peak signal-to-noise ratio (PSNR) and structural similarity index (SSIM) metrics further validates the fidelity and high SNR of our reconstruction. The ground truth is the direct imaging result obtained when the aperture's F-number is set to 2.8. Whether the spectral center is inside or outside the aperture, deviations from this tangential line result in a significant decline in PSNR and SSIM. Additionally, we consider reconstruction results to be unaffected if the PSNR and SSIM values exceed half of their peak values (in this experiment, the approximate range corresponds to deviations within 3% of the radius). Under these conditions, the reconstructed results still retain high resolution and image quality. The results of the MSKR-SAI method demonstrate its robustness in far-field imaging applications.

In this Letter, we have introduced macroscopic space-domain Kramers–Kronig relations synthetic aperture imaging as a novel approach to enhancing far-field resolution. By leveraging the aperture scanning characteristics of macroscopic imaging systems and the space-domain Kramers–Kronig relations, MSKR-SAI achieves non-iterative phase recovery, overcoming the limitations of conventional iterative methods. Simulations using the USAF resolution target demonstrated a twofold improvement in resolution, confirming the method's effectiveness in improving imaging quality. Furthermore, the robustness of MSKR-SAI was validated under varying measurement errors, demonstrating its resilience even when sub-aperture positions deviate to different extents. This capability ensures stable performance in practical applications, where precision may be affected by imperfections in the imaging system. MSKR-SAI represents a promising method for high-resolution, artifact-free far-field imaging, offering significant improvements in both reconstruction speed and imaging efficiency. In particular, we envision that by designing specific aperture shapes, MSKR-SAI may eventually integrate with a camera array to enable single-exposure non-iterative reconstruction. Currently, MSKR-SAI employs aperture scanning to achieve synthetic aperture imaging; however, we anticipate that with the integration of camera arrays and specifically designed aperture shapes, MSKR-SAI could evolve into a faster, non-iterative solution with enhanced temporal resolution, making it promising for dynamic or real-time applications.

Funding. National Natural Science Foundation of China (U21B2033, 61905115, 62105151, 62175109); National Major Scientific Instrument Development Project (62227818); Leading Technology of Jiangsu Basic Research Plan (BK20192003); Youth Foundation of Jiangsu Province (BK20190445, BK20210338); Biomedical Competition Foundation of Jiangsu Province (BE2022847); Key National Industrial Technology Cooperation Foundation of Jiangsu Province (BZ2022039); Fundamental Research Funds for the Central Universities (30920032101).

Disclosures. The authors declare no conflicts of interest.

Data availability. Data underlying the results presented in this Letter are not publicly available at this time but may be obtained from the authors upon reasonable request.

Supplemental document. See Supplement 1 for supporting content.

REFERENCES

1. G. Zheng, C. Shen, S. Jiang, *et al.*, Nat. Rev. Phys. **3**, 207 (2021).
2. G. Zheng, R. Horstmeyer, and C. Yang, Nat. Photonics **7**, 739 (2013).
3. L. Bian, J. Suo, G. Zheng, *et al.*, Opt. Express **23**, 4856 (2015).
4. X. Ou, G. Zheng, and C. Yang, Opt. Express **22**, 4960 (2014).
5. X. Wu, N. Zhou, Y. Chen, *et al.*, Light: Sci. Appl. **13**, 237 (2024).
6. Y. Shu, J. Sun, J. Lyu, *et al.*, PhotoniX **3**, 24 (2022).
7. S. Li, B. Wang, K. Liang, *et al.*, Adv. Photon. Res. **4**, 2300180 (2023).
8. P. Song, S. Jiang, T. Wang, *et al.*, Photonics Res. **10**, 1624 (2022).
9. S. Dong, R. Horstmeyer, R. Shiradkar, *et al.*, Opt. Express **22**, 13586 (2014).
10. J. Holloway, M. S. Asif, M. K. Sharma, *et al.*, IEEE Trans. Comput. Imaging **2**, 251 (2016).
11. J. Holloway, Y. Wu, M. K. Sharma, *et al.*, Sci. Adv. **3**, e1602564 (2017).
12. J. Wu, F. Yang, and L. Cao, Opt. Lasers Eng. **155**, 107068 (2022).
13. S. Li, B. Wang, H. Guan, *et al.*, Advanced Imaging **1**, 011005 (2024).
14. Y. Baek and Y. Park, Nat. Photonics **15**, 354 (2021).
15. Y. Baek, K. Lee, S. Shin, *et al.*, Optica **6**, 45 (2019).
16. X. Chang, C. Shen, S. Liu, *et al.*, Opt. Lett. **48**, 4161 (2023).
17. R. Cao, C. Shen, and C. Yang, Nat. Commun. **15**, 4713 (2024).
18. C. Shen, M. Liang, A. Pan, *et al.*, Photonics Res. **9**, 1003 (2021).
19. J. Oh, H. Hugonnet, and Y. Park, Nat. Commun. **14**, 4870 (2023).
20. R. Zhang, N. Zhou, H. Tang, *et al.*, Laser Photonics Rev. **18**, 2300770 (2024).
21. C. Zuo, J. Sun, J. Li, *et al.*, Sci. Rep. **7**, 7654 (2017).
22. J. Sun, C. Zuo, J. Zhang, *et al.*, Sci. Rep. **8**, 7669 (2018).
23. C. Lee, Y. Baek, H. Hugonnet, *et al.*, Opt. Lett. **47**, 1025 (2022).